The Meteoritical Society

Meteoritics & Planetary Science 58, Nr 12, 1747–1759 (2023)
doi: 10.1111/maps.14095

Chemical and genetic characterization of the ungrouped pallasite Lieksa

Emily M. CHIAPPE[1]*, Richard D. ASH[1], Arto LUTTINEN[2], Sari LUKKARI[3], Jukka KUVA[3], Connor D. HILTON[4], and Richard J. WALKER[1]

[1]Department of Geology, University of Maryland, College Park, Maryland, USA
[2]Finnish Museum of Natural History, University of Helsinki, Helsinki, Finland
[3]Geological Survey of Finland, Espoo, Finland
[4]Pacific Northwest National Laboratory, Richland, Washington, USA
*Correspondence
Emily M. Chiappe, Department of Geology, University of Maryland, College Park, MD 20742, USA.
Email: echiappe@umd.edu

(*Received 27 June 2023; revision accepted 09 October 2023*)

ABSTRACT–The meteorite Lieksa was found in 2017 in Löpönvaara, Finland, and later donated to the Finnish Museum of Natural History. Here, we report siderophile element concentrations, genetic isotopic data, and a metal–silicate segregation age for the meteorite. The ~280 g Lieksa is ~80% metal and ~20% silicate and oxide inclusions by volume, with the inclusions consisting primarily of Fe-rich olivine. Due to Lieksa's silicate content, coupled with a texture characterized by metal enclosing the silicates, it has been classified as a pallasite. Lieksa's olivine and bulk chemical characteristics are distinct from those of the known pallasite and iron meteorite groups, consistent with its classification as ungrouped. The meteorite exhibits a flat, chondrite-normalized highly siderophile element pattern, consistent with an origin as an early crystallization product from a metallic melt with chondritic relative abundances. Molybdenum, Ru, and ^{183}W isotopic data indicate that Lieksa formed in the non-carbonaceous (NC) domain of the solar nebula. Radiogenic ^{182}W abundances for Lieksa yield a model metal–silicate segregation age of 1.5 ± 0.8 Myr after calcium-aluminum-rich inclusion formation, which is within the range established for other NC-type pallasite and iron meteorite parent bodies.

INTRODUCTION

The Lieksa meteorite was found in Löpönvaara (63°24.382′ N, 30°04.227′ E), Finland, ~10 km NE of the town of Lieksa on May 30, 2017. Pekka Vallimies discovered the heavy, rust-covered rock while looking for false morel mushrooms and picked it up as a potential ore specimen. After removing the rust with a wire brush, Vallimies noticed that the ~280 g piece had the metallic sheen and pitted shape typical of meteorites and submitted the find to the Geological Survey of Finland (GTK). Examination led by Dr. Kari Kinnunen confirmed a meteoritic origin, and Vallimies donated it to the national meteorite collection of the LUOMUS Finnish Museum of Natural History on May 30, 2018. Numerous smaller pieces of metal-rich meteorites (up to 27.1 g) have been subsequently discovered in the find area, but have not yet been chemically characterized. Lieksa contains relatively Fe-rich (Fa_{23}) olivine inclusions which, along with their textural relationship with the metal, have led to the classification of Lieksa as a pallasite (Gattacceca et al., 2023). Pallasites are commonly thought to have formed through mixing of core and mantle materials at the metal–silicate interface, although the exact mechanisms behind this process are debated (e.g., Boesenberg et al., 2012; Walte et al., 2020; Wasson & Choi, 2003; Wood, 1978; Yang et al., 2010).

A key objective of this study is to assess whether Lieksa is related to any other meteorites. Metal-rich meteorites, including pallasites and irons, are often characterized with respect to their siderophile element concentrations, which can reveal shared chemical similarities

and differences within and between the established groups (e.g., Dauphas et al., 2002; McCoy et al., 2011; Pernicka & Wasson, 1987; Scott et al., 1973; Walker et al., 2008; Wasson & Choi, 2003). Furthermore, mass independent "genetic" isotope compositions of elements, such as Cr and Ti, can be used to assess whether chemically similar meteorites can potentially be related to a common parent body. Genetic isotope heterogeneities have been observed between bulk planetary materials that can broadly be divided into the non-carbonaceous- (NC) and carbonaceous chondrite- (CC) type domains, commonly interpreted to sample inner and outer solar system materials, respectively (e.g., Budde et al., 2016; Kruijer et al., 2017; Warren, 2011). Through the study of genetic isotope variations present in siderophile elements such as Ni, Mo, Ru, and W, as well as the application of the ^{182}Hf-^{182}W chronometer ($t_{½}$ = 8.9 Myr), used to constrain metal–silicate segregation ages, pallasites and iron meteorites have proven useful in advancing understanding of the origins and evolution of the early solar system (Dauphas et al., 2002; Fischer-Gödde et al., 2015; Kruijer et al., 2017, 2022; Regelous et al., 2008).

In this study, we report chemical and genetic isotopic characteristics of Lieksa. The element concentration data are utilized in order to assess possible relationships between Lieksa and the established pallasite and iron meteorite groups. Additionally, Mo, Ru, and W isotopic compositions are determined in order to characterize the genetic origins of Lieksa and the timing of metal–silicate segregation on its parent body.

MATERIALS AND METHODS

Tomography and Scanning Electron Microscopy

The main piece of Lieksa was examined at LUOMUS with a Nikon XTH 225 micro-CT instrument using 180 kV acceleration voltage, 500 μA current, 90 μm spot size, and 1 mm Sn filter. The x-ray beam was produced using a W target. The electron optical work was carried out at SEM Laboratory, GTK, Espoo, using a field emission scanning electron microscope (FE-SEM), model JEOL JSM-7100F Schottky and a Hitachi SU3900 SEM. The FE-SEM imaging was targeted on a carbon coated, polished sample under high vacuum conditions, whereas the SEM imaging of a sawn sample surface was conducted under low vacuum conditions. The run conditions were 20 kV acceleration voltages and 1 nA probe current and we used Aztec software for the analyses.

Siderophile Element and ^{187}Re-^{187}Os Isotopic Analysis

A 13 g cut piece of Lieksa was used for chemical and isotopic analyses at the University of Maryland (UMd). The sample was initially polished with sandpapers of diminishing grit size to ensure that the cut surface was removed of rust and blade markings. The sample was then ultrasonicated in ethanol prior to analysis in order to remove any remaining surficial contaminants. Concentrations of 17 siderophile elements (Re, Os, W, Ir, Mo, Ru, Pt, Rh, Ni, Co, Fe, Pd, As, Au, Cu, Ga, and Ge) were obtained by laser ablation-inductively coupled plasma-mass spectrometry (LA-ICP-MS). Siderophile element concentrations in the metal were obtained using a *New Wave UP213* ultraviolet laser coupled to a *Thermo Finnigan Element 2* ICP-MS. Five ~5 mm long laser ablation tracks were averaged in order to obtain a composition representative of Lieksa's metal. Data were processed using *LAMTRACE* (Rusk, 2009), using known concentrations of in-house laboratory reference iron meteorites Filomena, Hoba, and Coahuila. For each analysis, following blank subtraction, Fe + Ni + Co abundances were forced to sum to 100% (Campbell & Humayun, 2005).

Highly siderophile element (HSE; Re, Os, Ir, Ru, Pt, Pd) concentrations and ^{187}Re-^{187}Os systematics were determined for a bulk sample of Lieksa following the isotope dilution procedure outlined in Walker et al. (2008). In brief, a ~70 mg piece of Lieksa was cut from the larger piece and added to a *Pyrex*® Carius tube along with appropriate amounts (determined by LA-ICP-MS data) of a mixed spike containing ^{185}Re-^{190}Os, a separate mixed spike of ^{191}Ir-^{99}Ru-^{194}Pt-^{105}Pd, 2.5 mL of concentrated HCl, and 5 mL of concentrated HNO_3. The tube was then sealed and heated at ~220°C for 48 h to obtain sample spike. Osmium was then separated using the carbon tetrachloride (CCl_4) extraction method described in Cohen and Waters (1996), and further purified via microdistillation methods outlined in Birck et al. (1997). The resulting purified Os was loaded onto a Pt filament, along with a Ba hydroxide activator, and analyzed using a *Thermo Fisher Triton* thermal ionization mass spectrometer (TIMS) at UMd. Analyses were done in static mode using Faraday cup collectors. Measurements were taken in three blocks with 40 cycles/block for a total of 120 measurements (4 s integration per step). Osmium isotopic data were corrected for both instrumental mass fractionation by normalizing ^{190}Os/^{188}Os to 3.08271 (Allègre & Luck, 1980) and oxide interference.

The other HSE within the residual acid were separated and purified using a 1.5 mL anion exchange column (Rehkämper & Halliday, 1997). Rhenium and Ru were eluted with 12 mL of 6 M HNO_3, Pt and Ir with 13 mL of concentrated HNO_3, and Pd with 14 mL of concentrated HCl. The Re and Ru aliquot was further purified using an additional anion exchange column. Rhenium, Ru, Ir, Pt, and Pd were analyzed using a *Thermo Fisher Neptune Plus* multi-collector ICP-MS at

UMd. Tungsten was added to the Re aliquots to correct for mass fractionation effects. The blanks for this procedure measured 9, 4, 3, 45, 23, and 23 pg for Re, Os, Ir, Ru, Pt, and Pd, respectively. Blank corrections were applied but did not have a significant impact on the final HSE concentrations. Estimated measurement uncertainties for Re and Os are <0.1%, and ≤2% for the other HSE.

Molybdenum, Ru, W, Os, and Pt Isotopic Measurements

A ~2 g piece of Lieksa metal was cut, polished, and cleaned for Mo, Ru, W, Pt, and Os isotopic measurements. The piece was dissolved in 40 mL of 8 M HCl at ~140°C for 48 h in a *Teflon*® beaker. The solution was then divided into three aliquots that were processed separately following various methods. One aliquot was processed for Os for the purpose of cosmic ray exposure (CRE) assessment and correction. This was achieved following the same separation and purification techniques described in the previous section. Approximately 300 ng of Os was loaded onto a Pt filament along with a Ba hydroxide activator and analyzed using a *Thermo Fisher Triton* TIMS. Analyses were done in static mode using Faraday cup collectors. Measurements were taken in three blocks with 40 cycles/block for a total of 120 measurements (16 s integration per step). Osmium isotopic data were corrected for instrumental mass fractionation by normalizing $^{190}Os/^{188}Os$ to 3.08271 (Allègre & Luck, 1980). All isotopic compositions in this study are reported using the μ notation (e.g., Os):

$$\mu^{189}Os = \left(\frac{\frac{^{189}Os}{^{188}Os}_{sample}}{\frac{^{189}Os}{^{188}Os}_{standard}} - 1\right) \times 10^6$$

which corresponds to the part per million deviation of an isotopic ratio of a sample to that of a laboratory standard. Analytical uncertainties were assessed by measuring a laboratory standard multiple times during the analytical campaign and determining their external reproducibility (2SD). The 2SD for this campaign was ±6 ppm for $\mu^{189}Os$ ($n = 3$) based on measurements of the *Johnson Matthey* terrestrial laboratory standard.

A separate aliquot from the initial dissolution was processed for Mo, W, and Pt isotopic analyses following a scaled-up version of the anion exchange column procedure developed by Nagai and Yokoyama (2014). Tungsten was eluted from the column using 100 mL of 9 M HCl + 1 M HF, Mo was eluted using 50 mL of 6 M HNO_3 + 3 M HF, and Pt was eluted using 75 mL of concentrated HNO_3. The resulting Mo aliquot was dried, redissolved, and loaded onto a secondary anion exchange column following the column procedure outlined in Worsham et al. (2016). Molybdenum was eluted from the column using 12.5 mL of 1 M HCl, dried, and loaded onto the same column a second time to ensure purification. The aliquot was dried again and redissolved in 6 M HCl for loading. Approximately 1000 ng of Mo was loaded onto an outgassed Re filament along with 2 μL of a 5 μg μL^{-1} $La(NO_3)_3$ activator solution. A second filament was loaded with 2 μL of the 5 μg μL^{-1} La $(NO_3)_3$ activator following the double filament assembly described in Worsham et al. (2016). Molybdenum was analyzed as MoO^-_3 using a *Thermo Fisher Triton Plus* TIMS using a 3-peak jump, multi-dynamic method. Isotopic data were corrected for instrumental mass fractionation by normalizing $^{98}Mo/^{96}Mo$ to 1.453171 (Lu & Masuda, 1994). The 2SD for this campaign was ±37, ±12, ±8, ±4, and ±20 ppm for $\mu^{92}Mo$, $\mu^{94}Mo$, $\mu^{95}Mo$, $\mu^{97}Mo$, and $\mu^{100}Mo$, respectively, based on repeated measurements of the *Alfa Aesar* terrestrial laboratory standard ($n = 5$).

The W aliquot from the initial primary column was dried, redissolved in 0.4 M HCl + 0.5 M HF, and loaded onto a secondary anion exchange column following methods described in Nagai and Yokoyama (2014), wherein W was eluted with 9 M HCl + 3 M HF. The purified W aliquot was dried and redissolved in 0.4 M HCl + 0.5 M HF for loading. Approximately 1000 ng of W was loaded onto an outgassed Re filament along with 1 μL of 5 μg μL^{-1} La-5 μg μL^{-1} Gd activator solution and measured as WO^-_3 using a *Thermo Fisher Triton* TIMS following measurement techniques outline in Archer et al. (2017). Isotopic data were corrected for instrumental mass fractionation by normalizing $^{186}W/^{184}W$ to 0.92767 (Völkening et al., 1991). The 2SD for this analytical campaign was ±6 ppm for $\mu^{182}W$ and ± 3 ppm for $\mu^{183}W$ based on repeated measurements of the *Alfa Aesar* terrestrial laboratory standard ($n = 5$).

The Pt aliquot from the initial primary column was dried, redissolved in a 2:1 mixture of concentrated HNO_3 and HCl, and refluxed overnight at 100°C, following the purification procedure described in Hunt et al. (2017). The aliquot was then dried and refluxed overnight once more in 1 M HCl, then diluted with ascorbic acid for loading onto an anion exchange column, where Pt was eluted with 15 mL of concentrated HNO_3. This clean-up procedure was repeated once more to ensure Pt-Ir separation. The solution was dried, treated with $HClO_4$, and refluxed overnight in 2:1 HNO_3 and HCl to remove organics and Os. The sample was dissolved in 2% HNO_3 to be analyzed on a *Thermo Fisher Neptune Plus* multi-collector ICP-MS. Isotopic data were corrected for instrumental mass fractionation by normalizing $^{198}Pt/^{195}Pt$ to 0.21450 (Kruijer et al., 2013). The 2SD for this analytical campaign, as defined by repeated analyses of the *Alfa Aesar* laboratory standard, was ±8 ppm for $\mu^{196}Pt$ ($n = 20$).

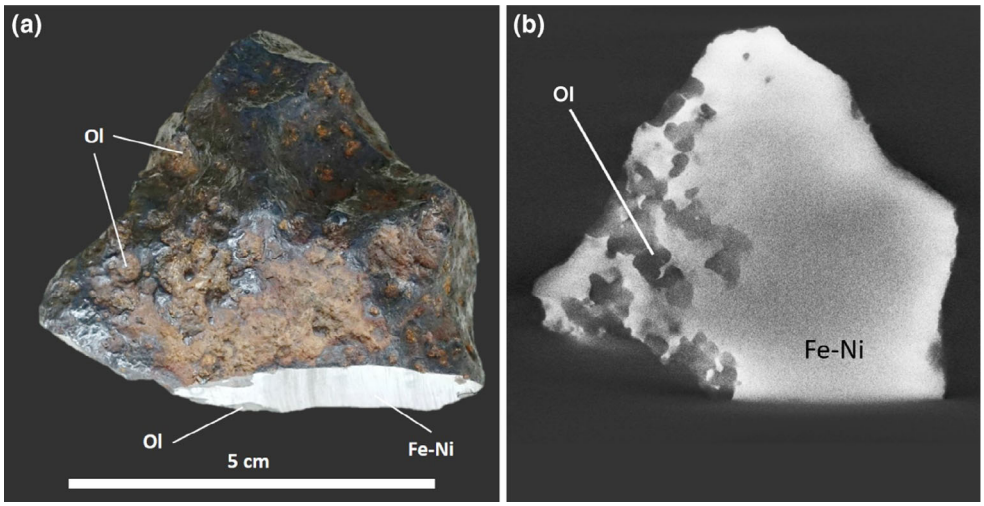

FIGURE 1. Photograph (a) and micro-CT cross section (b) of Lieksa. Light gray is Fe-Ni metal and dark regions are olivine and oxide inclusions. (Color figure can be viewed at wileyonlinelibrary.com)

The third aliquot from the initial sample digestion was processed for Ru following purification techniques outlined in Bermingham et al. (2016). The aliquot was dried and redissolved in 0.15 M HCl for loading onto a primary cation column. Ruthenium was eluted with 15 mL of 0.15 M HCl and further purified via microdistillation using 0.2 g mL^{-1} CrO_3 in 0.5 M H_2SO_4 and 4 M HBr. The sample was then taken up in 5% HNO_3 and analyzed using a *Thermo Fisher Neptune Plus* multi-collector ICP-MS. Isotopic data were corrected for instrumental mass fractionation by normalizing $^{99}Ru/^{101}Ru$ to 0.745075 (Chen et al., 2010). The 2SD external precision for this analytical campaign was ±8 ppm for $\mu^{100}Ru$ based on repeated measurements of the *Alfa Aesar* laboratory standard (n = 15).

RESULTS

Petrography

Lieksa's original mass of ~280 g was reduced to 238.30 g after the removal of the rusty surface by the finder. The size of the cleaned piece was 65.9 × 59.8 × 29.9 mm before cutting for geochemical analyses. The overall irregular appearance of Lieksa is typical of metal-rich meteorites (Figure 1a). Inclusions and remnants of the weathered crust are discernible on the pitted surface of the meteorite as reddish-brown patches within the dark grayish metal. At least some of the shallow indentations and pits may be regmaglypts, but long exposure to weathering, possible glacial transportation, and the removal of the rusty surface by the finder may have had a strong influence on the surface features.

Olivine is found in the small indentations of the weathered surface and on the cut surface (Figure 1a). Initial x-ray tomographic examination revealed that the meteorite consists of ~80 vol% metal and ~20 vol% silicate and oxide inclusions (Gattacceca et al., 2023). Tomographic scanning shows that the inclusions are unevenly distributed with most inclusions concentrated near the surface of the sample (Figure 1b). Observations on the surfaces and the results of tomographic scanning suggest the inclusions are predominantly rounded olivine up to ~10 mm in diameter. Minor quantities of Cr-Fe-Al-spinel are found adjacent to and within olivine grains (Figure 2a). Backscattered electron (BSE) images of the ataxitic Fe-Ni metal show micro-Widmanstätten texture with kamacite band widths varying mainly from 4 to 20, and up to 40 μm in rare platelets (Figure 2b). Decomposition of taenite to duplex plessite also occurs (Figure 2b). Troilite occurs as small inclusions (<10 μm) in the metal phase (Figure 2b). Olivine and spinel have rounded, lobate boundaries with metal, typical of many pallasites (Figure 2a). Weathering of metal to iron oxides, particularly on the metal–silicate boundaries, can also be seen (Figure 2a).

Bulk Compositional Analysis by LA-ICP-MS and HSE Concentrations

Bulk siderophile element concentrations and their 2SD variations determined by LA-ICP-MS are reported in Table 1. The data for individual laser ablation tracks are provided in Table S1. The siderophile element data, normalized to CI chondrite, are shown in Figure 3. Lieksa exhibits a moderate depletion in the volatile siderophile elements (e.g., Ga and Ge) relative to the

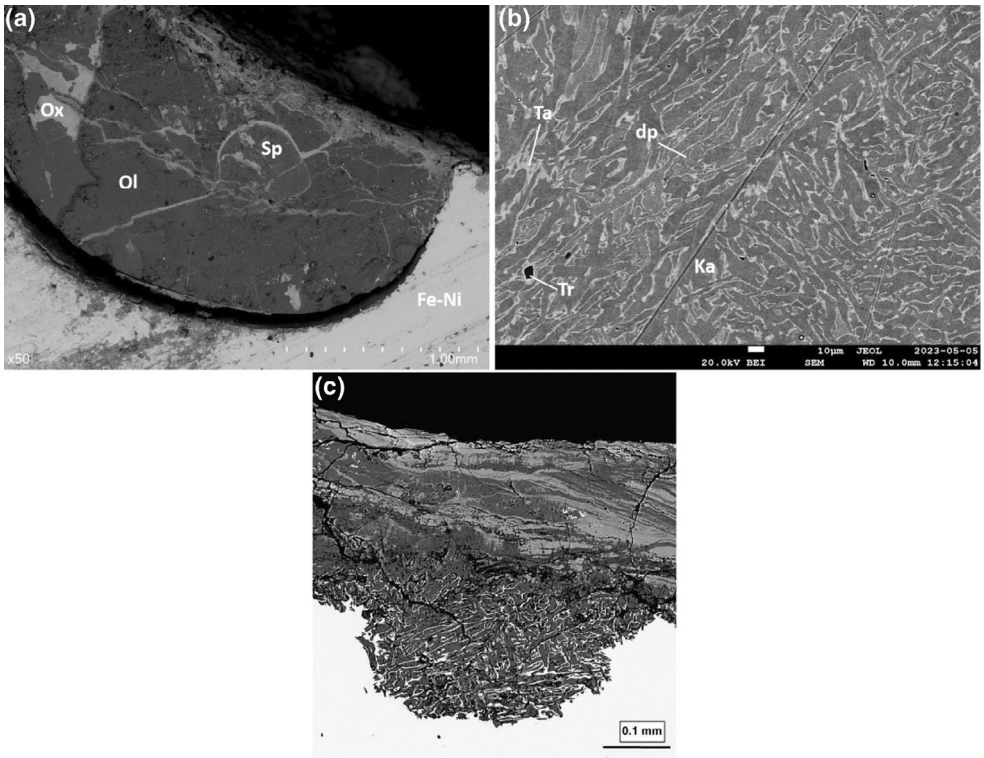

FIGURE 2. (a) BSE image showing inclusions (Ol: olivine; Ox: oxide, Sp: spinel). Secondary Fe-oxide mineralization occurs along metal–silicate boundaries, in olivine-hosted veins, and on the surface. (b) BSE image of duplex plessite textures in Fe-Ni metal (Ka: kamacite; Ta: taenite, Tr: troilite, dp: duplex plessite). (c) BSE image showing the vertical section through the surface of Lieksa. Upper stratified layers are weathering crust and rind. Fusion crust with vermicular Fe-Ni (taenite) in iron oxide was preserved in microscopic pits. The light, lower area is Fe-Ni metal.

more refractory siderophile elements (e.g., Mo and W). Figure 4a–c shows Ga, Ge, and Ir abundances plotted against Ni, with pallasite and iron meteorite groups for comparison. HSE concentrations and Re-Os isotopic data for a bulk sample of Lieksa metal are reported in Table 2. Lieksa exhibits a flat chondrite-normalized HSE pattern, with a slight depletion in Pd, similar to patterns exhibited by relatively unfractionated irons and pallasites from some of the established groups (Figure 5 and Figure S1). On a $^{187}Re/^{188}Os$ versus $^{187}Os/^{188}Os$ diagram, Lieksa plots ~0.5% above a 4.56 Ga reference isochron, indicating minor post-crystallization open-system behavior of HSE (Figure S2).

Isotopic Compositions

Platinum and Os isotopic data were obtained in order to assess, and correct for possible CRE effects. CRE can result in neutron capture reactions in meteorites, thereby modifying Mo, Ru, and W isotopic compositions (Kruijer et al., 2013; Wittig et al., 2013). These effects can be monitored and corrected for through utilization of Pt and Os dosimeters, as $\mu^{196}Pt$ and $\mu^{189}Os$ values are expected to increase and decrease, respectively, with continued cosmic ray flux (Walker, 2012; Wittig et al., 2013). Platinum and Os isotopic compositions for Lieksa are reported in Table 3. Lieksa has a $\mu^{196}Pt$ value of 7 ± 8 ($n = 3$) and a $\mu^{189}Os$ value of -3 ± 6 ($n = 4$). Neither isotopic composition displays a resolved deviation from the laboratory standards, indicating that the isotopic data reported here do not require correction for CRE effects. Mass independent Mo, Ru, and W isotopic data for Lieksa are also reported in Table 3.

DISCUSSION

Chemical Relations to Pallasite and Iron Meteorite Groups

The kamacite band widths and duplex plessite texture observed in Lieksa occur in both pallasites and iron meteorites and are compatible with Ni concentrations of <13 wt% in the metal (Goldstein & Michael, 2006; McCoy et al., 2019; Zhang et al., 1993). The abundance

TABLE 1. Average ($n = 5$) siderophile element concentrations for Lieksa obtained via LA-ICP-MS.

	Concentration	2SD
Re	0.56	0.08
Os	7.4	0.87
W	1.3	0.52
Ir	6.8	0.37
Mo	12	3.5
Ru	9.4	0.88
Pt	12.4	0.90
Rh	1.4	0.09
Ni	10	1.9
Co	0.70	0.38
Fe	89	2.9
Pd	2.9	0.28
As	4.7	0.54
Au	0.67	0.46
Ga	2.1	0.13
Ge	58	2.6

Note: Iron, Ni, and Co concentrations reported in wt%, all other elements reported in ppm.

of olivine is lower than in most pallasites (>35 vol%; Buseck, 1977), suggesting that Lieksa may represent the more metal-rich end of the iron meteorite–pallasite continuum. Judging from the concentration of inclusions near the surfaces, however, the low olivine-metal ratio may also be a result of the small sample size and the heterogenous nature of pallasites, such as has been observed with respect to the pallasite Seymchan (van Nierkirk et al., 2007). Olivine in Lieksa is more Fe-rich (~Fa_{23}; Gattacceca et al., 2023) than olivine found in main group pallasites (PMG; $Fa_{11–13}$) and Eagle Station pallasites (PES; $Fa_{19–20}$; Buseck & Goldstein, 1969), as well as the ungrouped pallasite Gyarub Zangbo ($Fa_{21.6}$; Gattacceca et al., 2022; Jiang et al., 2023), consistent with formation under relatively oxidizing conditions.

Pallasites and iron meteorites are classified based on concentrations of the refractory and moderately refractory siderophile elements Ir and Ni, and the volatile siderophile elements Ga and Ge, as well as textural characteristics and accessory phases (e.g., Scott et al., 1973; Wasson & Wai, 1976). While Lieksa shares some chemical and textural characteristics with certain pallasite and iron groups, it is not a good match to any known group. For example, while the Ga concentration of Lieksa is similar to the group IVA irons, its Ge concentration is substantially higher, and more similar to the IIC, IID, and IIF magmatic iron groups, as well as the IAB-sHL subgroup and PMG (Figure 4). Most pallasites are classified as PMG and likely belong to the same parent body (Clayton & Mayeda, 1996; Greenwood et al., 2015; Wasson & Choi, 2003). The PES and the pyroxene pallasites (PXPs) are groups with many fewer members. Several pallasites have been classified as ungrouped, including Milton, Choteau, and Gyarub Zangbo, based on chemical, textural, and genetic isotope compositions (Buchwald, 1975; Clayton & Mayeda, 1996; Hilton et al., 2020; Kracher et al., 1980; McCoy et al., 2019). Lieksa does not exhibit similar chemical characteristics to any ungrouped pallasites or irons (Figure S3). Lieksa is therefore classified as ungrouped due to the lack of overlap in chemical composition with known pallasite and iron groups, as well as other ungrouped pallasites.

Although ungrouped, similarities in chemical composition of some elements to other pallasite and iron groups may lead to important insights to Lieksa's parent body formational and evolutionary histories. The iron meteorite groups with overall siderophile element abundance patterns most closely resembling that of Lieksa are the group IIC, IID, and IIF irons (Figure 3). In addition to their comparable Ge concentrations, they also exhibit similar Ir concentrations (Figure 4), as well as similar moderately to highly refractory siderophile elements (e.g., Ni, Co, Mo, W) abundances. Some of these elements (e.g., Ni, Ge, Mo) are characterized by solid metal–liquid metal partition coefficients near 1, so they would not be expected to vary substantially within the crystallization sequence of a specific group. These similarities also extend to their HSE patterns, with Lieksa exhibiting a pattern similar to that of the least fractionated members of each of the IIC, IID, and IIF groups, as well as to the PMG Pavlodar (Figure 5 and Figure S1). These similarities in the relative abundances of HSE suggest that the chemical starting compositions of the parent bodies were similar and broadly chondritic. The similar absolute concentrations also suggest that the mass proportion of core to silicate mantle for Lieksa was similar to these irons.

Despite some chemical similarities shared with certain pallasite and iron groups, the overall siderophile element pattern for Lieksa is unique. Lieksa exhibits a flatter overall pattern across most refractory siderophile elements, compared to other pallasites and irons, as well as an unusually high Ge/Ga ratio of 28. Germanium/Ga ratios greater than 10 are uncommon, with most magmatic iron groups, the non-magmatic IAB complex, and PMG exhibiting Ge/Ga ratios lower than 5. Although the IIF magmatic irons, the PES, and a handful of ungrouped iron meteorites (Kracher et al., 1980; Olsen et al., 1996) are characterized by Ge/Ga >5, the ratios of 12 and 14 exhibited by the IIF irons and PES, respectively, remain significantly lower than that of Lieksa. Of the ungrouped pallasites and iron meteorites, the iron meteorite Emsland exhibits Ga and Ge concentrations closest to Lieksa, but still has a much lower Ge/Ga ratio of 12 (Buchwald, 1975; Figure S3). One possible explanation for the high Ge/Ga is that under conditions of metal segregation in the Lieksa

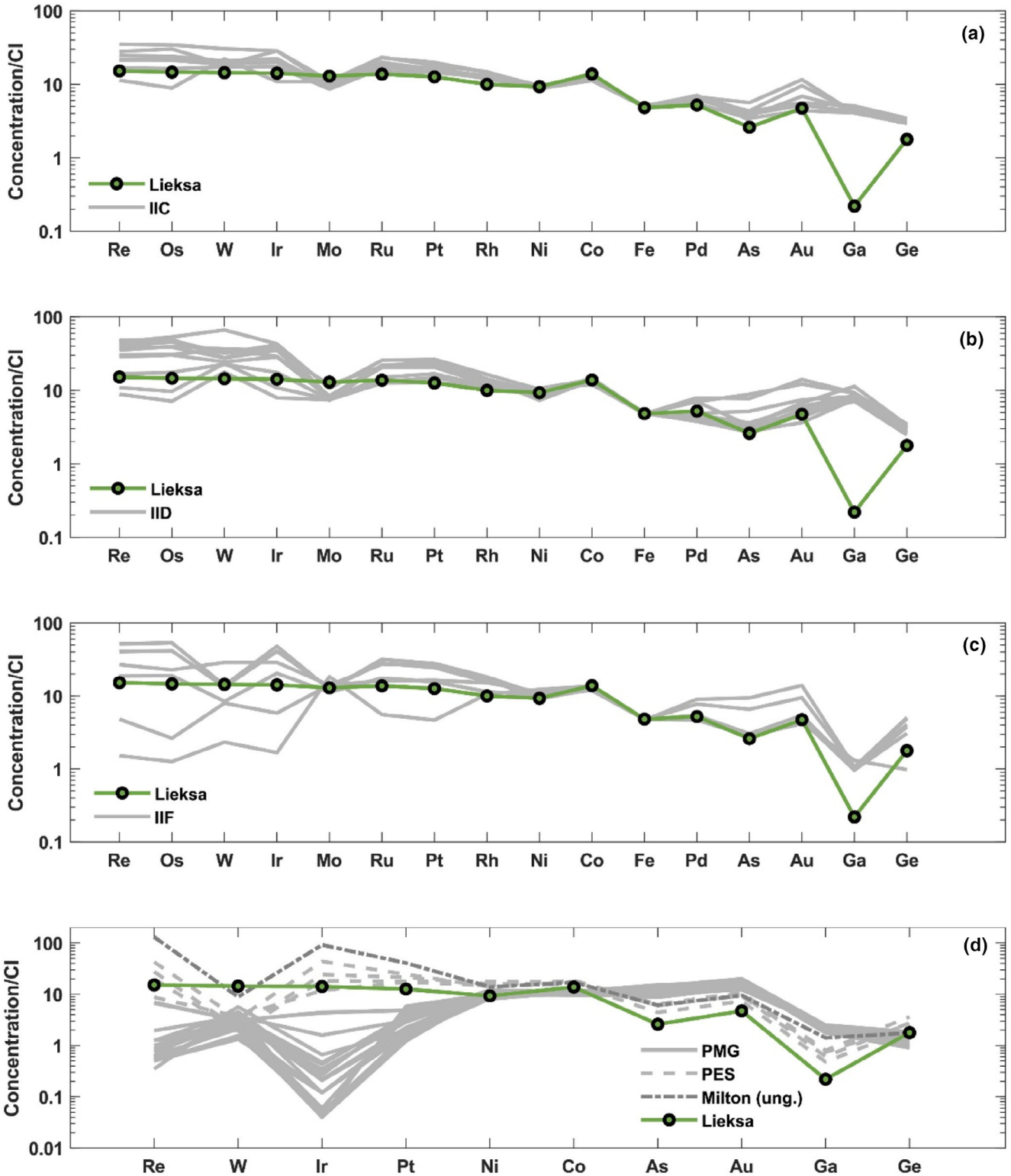

FIGURE 3. CI chondrite-normalized siderophile element abundances of Lieksa compared to the IIC (a), IID (b), and IIF (c) iron meteorite groups and the PMG, PES, and the ungrouped pallasite Milton (d). Elements are arranged in order of decreasing 50% condensation temperature from left to right (Lodders, 2003). Group data compiled from Wasson and Choi (2003), McCoy et al. (2019), Tornabene et al. (2020), Hilton et al. (2020), and Table S2. (Color figure can be viewed at wileyonlinelibrary.com)

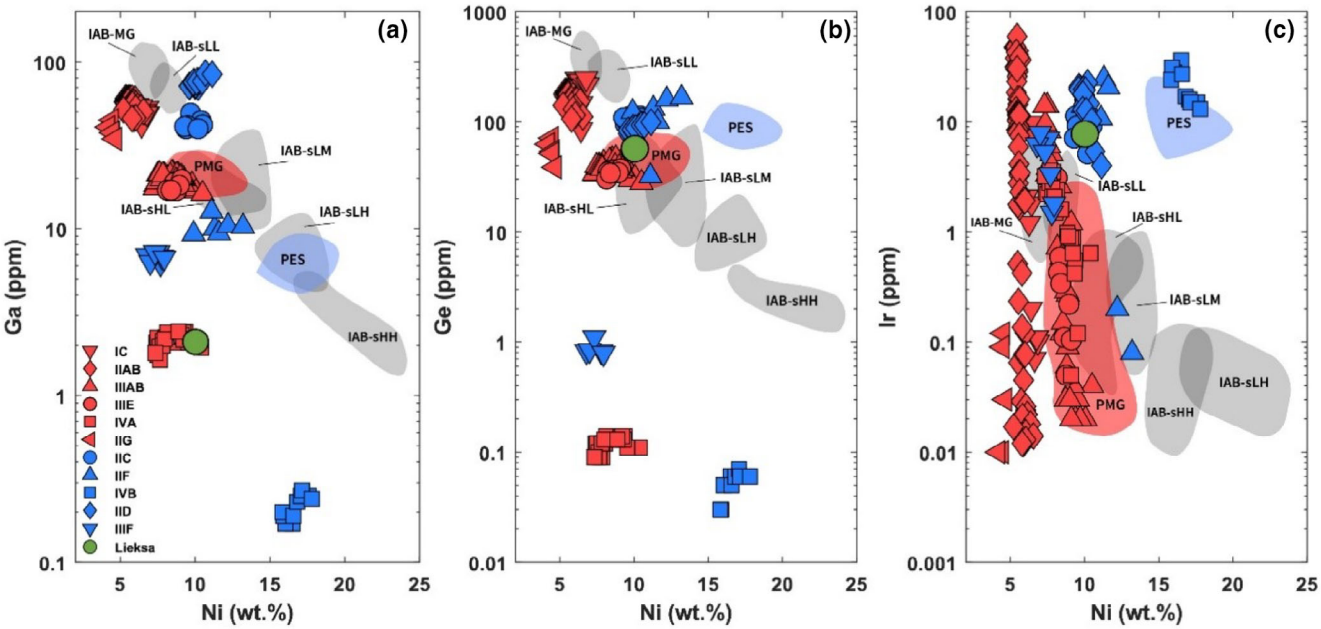

FIGURE 4. Compilation of Ga (ppm) versus Ni (wt%) (a), Ge (ppm) versus Ni (wt%) (b), and Ir (ppm) versus Ni (wt%) (c) for the magmatic iron meteorite groups, IAB complex subgroups, main group pallasites (PMG), Eagle Station pallasites (PES), and Lieksa. Red symbols are NC-type meteorites and blue symbols are CC-type meteorites. Lieksa is represented with a green circle. Data compiled from Schaudy and Wasson (1972), Scott et al. (1973), Buchwald (1975), Scott and Wasson (1976), Wasson and Kallemeyn (2002), Wasson and Choi (2003), Wasson and Huber (2006), Wasson et al. (2007), Wasson and Choe (2009), Hilton et al. (2020), Tornabene et al. (2020), and Table S2. (Color figure can be viewed at wileyonlinelibrary.com)

TABLE 2. Highly siderophile element concentrations and Re-Os systematics of Lieksa.

Wt (g)	Re	Os	Ir	Ru	Pt	Pd	$^{187}Re/^{188}Os$	2SD	$^{187}Os/^{188}Os$	2SD	ΔOs	2SD
0.0727	601.6	7991	7768	10,240	13,760	3445	0.3625	0.0005	0.12452	0.00012	+5.5	1.3

All concentrations are in ppb.

parent body Ga was considerably less siderophile (more lithophile) than Ge leading to the formation of metals with high Ge/Ga. This may reflect a higher oxidation state for the Lieksa parent body (Blanchard et al., 2015). Such a process is recorded in similarly high Ge/Ga ratios in chondritic magnetic separates (Kracher et al., 1980). Consistent with this, the HSE abundances of Lieksa are also similar to those of irons interpreted to sample relatively oxidized parent bodies, such as irons from the CC-type IIC, IID, and IIF groups (Hilton et al., 2022; Tornabene et al., 2020).

Relation to NC and CC Domains

Molybdenum, Ru, and ^{183}W isotopic differences recorded between different pallasites and iron meteorites have been attributed to the heterogenous accretion of isotopically diverse precursor materials, composed of variable contributions of *p*-, *r*-, and *s*-process nuclides. These heterogeneities are utilized in assessing a meteorite's genetic heritage and in classifying meteorites as originating in the NC- or CC-type domain. These isotopic fingerprints are also useful in relating individual meteorites to established groups. The Mo, Ru, and ^{183}W isotopic compositions obtained for Lieksa fall within the range of compositions established for NC-type meteorites (Figure 6). NC type meteorites exhibit Mo isotopic compositions characterized by *s*-process depletions and *r*-process enrichments relative to terrestrial standards, although not as strong as those observed in CC-type meteorites (Budde et al., 2019; Spitzer et al., 2020). The Mo isotopic composition of Lieksa is comparable to most other NC meteorites (e.g., Bermingham et al., 2018; Kruijer et al., 2022; Worsham et al., 2019). Additionally, NC-type meteorites are characterized by linear Mo-Ru relationships for some isotopes (Figure 6b), as seen on previously published $\mu^{97}Mo$ versus $\mu^{100}Ru$ and $\mu^{92}Mo$ versus $\mu^{100}Ru$ plots (Dauphas et al., 2004; Fischer-Gödde et al., 2015; Tornabene et al., 2020). In contrast, CC-type meteorites do not exhibit this correlation. The $\mu^{100}Ru$

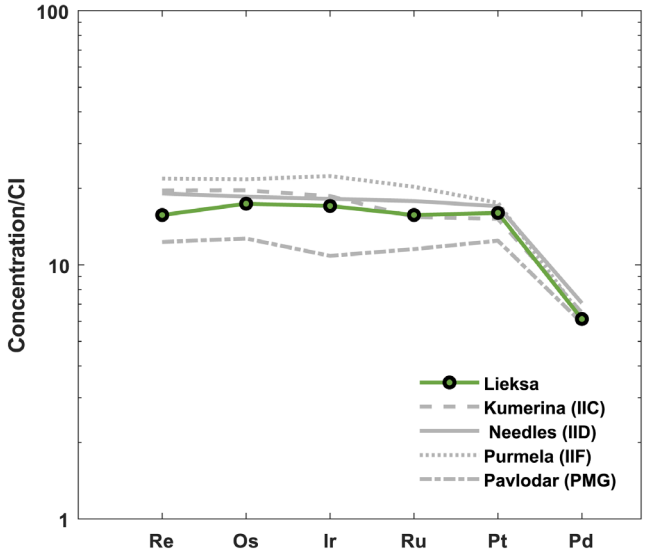

FIGURE 5. CI chondrite-normalized HSE abundances for Lieksa obtained via isotope dilution. Irons with similar HSE abundances from the IIC, IID, and IIF groups are included for comparison (Hilton et al., 2020, 2022; Tornabene et al., 2020). The main group pallasite (PMG) Pavlodar is also included (Table S3). Bulk composition data were normalized to concentrations obtained for the CI chondrite Orgueil (Horan et al., 2003). (Color figure can be viewed at wileyonlinelibrary.com)

TABLE 3. Platinum, Os, Mo, Ru, and W isotopic compositions of Lieksa. ΔT_{CAI}—Myr following CAI formation.

Isotopic composition	*n*	Value
$\mu^{196}Pt$	3	7 ± 8
$\mu^{189}Os$	4	−3 ± 6
$\mu^{92}Mo$	3	75 ± 37
$\mu^{94}Mo$	3	79 ± 12
$\mu^{95}Mo$	3	37 ± 8
$\mu^{97}Mo$	3	24 ± 4
$\mu^{100}Mo$	3	5 ± 20
$\mu^{100}Ru$	3	−55 ± 8
$\mu^{182}W_{Measured}$	2	−332 ± 6
$\mu^{183}W_{Measured}$	2	1 ± 3
ΔT_{CAI}		1.5 ± 0.5

Note: *n* is number of analyses. Uncertainties reflect 2SD of the standards run during each analytical campaign.

value obtained for Lieksa falls at the low end of the trend established by NC-type meteorites (Figure 6b). Furthermore, the $\mu^{183}W$ obtained here is similar to that of the terrestrial standard, which is also characteristic of NC-type meteorites (Figure 6c; Kruijer et al., 2017). Taken together, the combined Mo, Ru, and ^{183}W data are consistent with the interpretation that Lieksa is a typical NC-type meteorite, further distinguishing it from its closest chemical counterparts, the CC-type IIC, IID, and IIF irons and PES.

Metal–Silicate Segregation Age

The ^{182}Hf-^{182}W ($t_{1/2}$ = 8.9 Myr; Vockenhuber et al., 2004) system is often utilized in the study of metal-bearing meteorites in order to assess metal–silicate segregation time scales. Application of the system is based on the moderately siderophile nature of W and the lithophile nature of Hf. Due to their respective partitioning behaviors, as the core forms and as metal–silicate segregation proceeds, Hf will remain in the silicate portion of the melt, while W will preferentially partition into the metallic portion of the melt. At this point, no more ^{182}W can be produced in the core due to the absence of ^{182}Hf. The ^{182}W isotopic composition recorded in iron meteorites, therefore, reflects the ^{182}W composition at time of metal–silicate segregation. A model core formation age can then be calculated using the present-day chondritic $\mu^{182}W$ value of −191 ± 8 (Kleine et al., 2004), and the $\mu^{182}W$ value of CAI, −349 ± 7, which is used as a proxy for the W composition of the initial solar system (Kruijer et al., 2014). The average $\mu^{182}W$ value recorded by Lieksa is −332 ± 6, which corresponds to a model core formation age of 1.5 ± 0.8 Myr after CAI (Figure 6c). This age falls within the range established by NC-type pallasite and magmatic iron meteorite parent bodies.

CONCLUSIONS

Lieksa comprises ~80 vol% metal and ~20 vol% silicate and oxide inclusions, with the silicate phases consisting primarily of rounded olivine, leading to the classification of Lieksa as a pallasite (Gattacceca et al., 2023). Tomographic imaging indicates notable heterogeneity and distribution of the inclusions mostly close to the surfaces, which, along with the small mass of the meteorite, makes distinction between iron and pallasite problematic. Within the metal phases are duplex plessite textures as well as small troilite inclusions. Notably, Fe-rich olivine (Fa_{23}) sets Lieksa apart from known pallasites (Gattacceca et al., 2023). Lieksa's siderophile element abundances reveal a remarkably flat, CI chondrite-normalized pattern, with moderate depletions in the volatile siderophile elements that are distinct from those of the known pallasite and iron meteorite groups, although some similarities are shared with the CC IIC, IID, and IIF irons, as well as with the PES. Additionally, Lieksa's HSE pattern suggests it to be an early-formed crystallization product from a parent melt with chondritic relative abundances of HSE. Nucleosynthetic Mo, Ru, and W isotopic compositions indicate that Lieksa is an NC-type meteorite, and radiogenic ^{182}W values indicate that the parent body Lieksa samples underwent

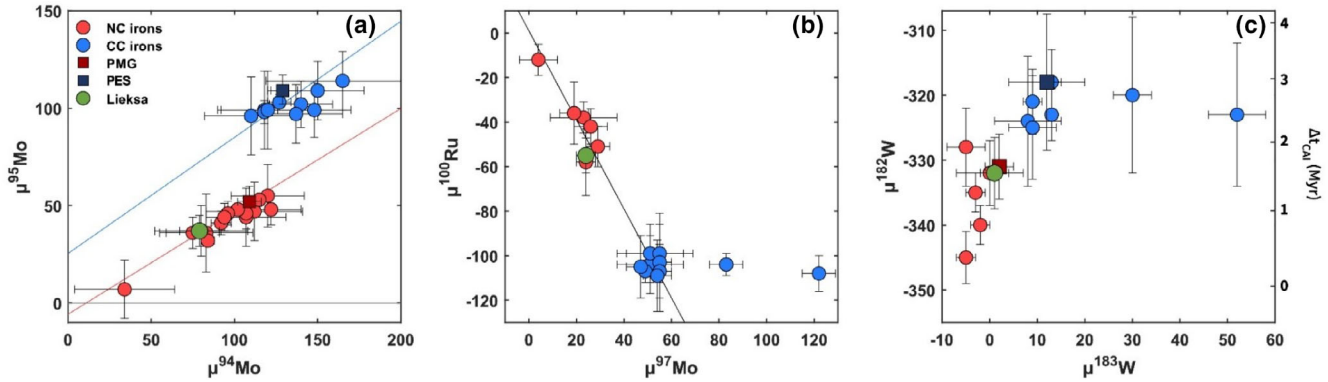

FIGURE 6. Compilation of μ^{94}Mo versus μ^{95}Mo (a), μ^{97}Mo and μ^{100}Ru (b), and μ^{183}W versus μ^{182}W (c) data for iron meteorites and pallasites. Blue symbols represent CC-type meteorites and red symbols represent NC-type meteorites. Red and blue lines represent NC and CC lines reported by Spitzer et al. (2020) and Budde et al. (2019), respectively. The black line represents the regression of the Mo-Ru correlation from Bermingham et al. (2018). Molybdenum data compiled from Bermingham et al. (2018), Worsham et al. (2019), Hilton et al. (2019), and Kruijer et al. (2022). Ruthenium data compiled from Worsham et al. (2019), Bermingham et al. (2018), and Hilton et al. (2019). Tungsten data compiled from Kruijer et al. (2017), Hilton et al. (2019), and Kruijer et al. (2022). Data for Lieksa are represented by the green circles. (Color figure can be viewed at wileyonlinelibrary.com)

metal–silicate segregation at 1.5 ± 0.8 Myr after CAI formation. Taken together, Lieksa's siderophile element concentrations, particularly its unusually high Ge/Ga ratio, fayalitic olivine, and genetic isotope compositions indicate that it originates from a previously unsampled NC-type parent body with an oxidation state more similar to that of CC planetesimals.

Acknowledgments—We gratefully acknowledge Lassi Pakkanen, Kari Kinnunen, Satu Vuoriainen, Hugh O'Brien, and Emma Bullock, respectively, for access to results of preliminary microanalyses, petrological observations, petrophysical measurements, LA-ICP-MS measurements, and BSE imaging that supported our study. Max Soderholm kindly performed micro-CT scanning of Lieksa at LUOMUS. Joe Boesenberg and an anonymous reviewer are thanked for their helpful comments to improve the manuscript. This work was supported by NASA Emerging Worlds grant 80NSSC20K0335 (to RJW).

Data Availability Statement—The data that support the findings of this study are available in the supplementary material of this article.

Editorial Handling—Dr. Marc W. Caffee

REFERENCES

Allègre, C. J., and Luck, J. M. 1980. Osmium Isotopes as Petrogenetic and Geological Tracers. *Earth and Planetary Science Letters* 48: 148–154.

Archer, G. J., Mundl, A., Walker, R. J., and Worsham, E. A. 2017. High-Precision Analysis of $^{182}W/^{184}W$ and $^{183}W/^{184}W$ by Negative Thermal Ionization Mass Spectrometry: Per-Integration Oxide Corrections Using Measured $^{18}O/^{16}O$. *International Journal of Mass Spectrometry* 414: 80–86.

Bermingham, K. R., Walker, R. J., and Worsham, E. A. 2016. Refinement of High Precision Ru Isotope Analysis Using Negative Thermal Ionization Mass Spectrometry. *International Journal of Mass Spectrometry* 403: 15–26.

Bermingham, K. R., Worsham, E. A., and Walker, R. J. 2018. New Insights into Mo and Ru Isotope Variation in the Nebula and Terrestrial Planet Accretionary Genetics. *Earth and Planetary Science Letters* 487: 221–29.

Birck, J. L., Barman, M. R., and Capmas, F. 1997. Re-Os Isotopic Measurements at the Femtomole Level in Natural Samples. *Geostandard Newsletter* 21: 9–27.

Blanchard, I., Badro, J., Siebert, J., and Ryerson, F. J. 2015. Composition of the Core from Gallium Metal-Silicate Partitioning Experiments. *Earth and Planetary Science Letters* 427: 191–201.

Boesenberg, J. S., Delaney, J. S., and Hewins, R. H. 2012. A Petrological and Chemical Reexamination of Main Group Pallasite Formation. *Geochimica et Cosmochimica Acta* 89: 134–158.

Buchwald, V. F. 1975. *Handbook of Iron Meteorites*. Berkeley: University of California Press. 1418.

Budde, G., Burkhardt, C., Brennecka, G. A., Fischer-Godde, M., Kruijer, T. S., and Kleine, T. 2016. Molybdenum Isotopic Evidence for the Origin of Chondrules and a Distinct Heritage of Carbonaceous and Non-Carbonaceous Meteorites. *Earth and Planetary Science Letters* 454: 293–303.

Budde, G., Burkhardt, C., and Kleine, T. 2019. Molybdenum Isotopic Evidence for the Late Accretion of Outer Solar System Material to Earth. *Nature Astronomy* 3: 736–741.

Buseck, P. R. 1977. Pallasite Meteorites—Mineralogy, Petrology and Geochemistry. *Geochimica et Cosmochimica Acta* 41: 711–740.

Buseck, P. R., and Goldstein, J. I. 1969. Olivine Compositions and Cooling Rates of Pallasitic Meteorites. *GSA Bulletin* 80: 2141–58.

Campbell, A. J., and Humayun, M. 2005. Composition of Group IVB Irons and their Parental Melt. *Geochimica et Cosmochimica Acta* 69: 4733–44.

Chen, J. H., Papanastassiou, D. A., and Wasserburg, G. J. 2010. Ruthenium Endemic Isotope Effects in Chondrites and Differentiated Meteorites. *Geochimica et Cosmochimica Acta* 74: 3851–62.

Clayton, R. N., and Mayeda, T. K. 1996. Oxygen Isotope Studies of Achondrites. *Geochimica et Cosmochimica Acta* 60: 1999–2017.

Cohen, A. S., and Waters, F. G. 1996. Separation of Osmium from Geological Materials by Solvent Extraction for Analysis by Thermal Ionisation Mass Spectrometry. *Analytica Chimica Acta* 332: 269–275.

Dauphas, N., Davis, A. M., Marty, B., and Reisberg, L. 2004. The Cosmic Molybdenum-Ruthenium Isotope Correlation. *Earth and Planetary Science Letters* 226: 465–475.

Dauphas, N., Marty, B., and Reisberg, L. 2002. Molybdenum Evidence for Inherited Planetary Scale Isotope Heterogeneity of the Protosolar Nebula. *The Astrophysical Journal* 565: 640–44.

Fischer-Gödde, M., Burkhardt, C., Kruijer, T. S., and Kleine, T. 2015. Ru Isotope Heterogeneity in the Solar Protoplanetary Disk. *Geochimica et Cosmochimica Acta* 168: 151–171.

Gattacceca, J., McCubbin, F. M., Grossman, J., Bouvier, A., Chabot, N. L., D'Orazio, M., Goodrich, C., et al. 2022. The Meteoritical Bulletin, No. 110. *Meteoritics & Planetary Science* 57: 2102–5.

Gattacceca, J., McCubbin, F. M., Grossman, J., Bouvier, A., Chabot, N. L., D'Orazio, M., Goodrich, C., et al. 2023. The Meteoritical Bulletin, No. 112. *Meteoritics & Planetary Science*. in press.

Goldstein, J. I., and Michael, J. R. 2006. The Formation of Plessite in Meteoritic Metal. *Meteoritics & Planetary Science* 41: 553–570.

Greenwood, R. C., Barrat, J.-A., Scott, E. R. D., Haack, H., Buchanan, P. C., Franchi, I. A., Yamaguchi, A., Johnson, D., Bevan, A. W. R., and Burbine, T. H. 2015. Geochemistry and Oxygen Isotope Composition of Main-Group Pallasites and Olivine-Rich Clasts in Mesosiderites: Implications for the "Great Dunite Shortage" and HED-Mesosiderite Connection. *Geochimica et Cosmochimica Acta* 169: 115–136.

Hilton, C. D., Ash, R. D., and Walker, R. J. 2020. Crystallization Histories of the Group IIF Iron Meteorites and Eagle Station Pallasites. *Meteoritics & Planetary Science* 55: 2570–86.

Hilton, C. D., Ash, R. D., and Walker, R. J. 2022. Chemical Characteristics of Iron Meteorite Parent Bodies. *Geochimica et Cosmochimica Acta* 318: 112–125.

Hilton, C. D., Bermingham, K. R., Walker, R. J., and McCoy, T. J. 2019. Genetics, Crystallization Sequence, and Age of the South Byron Trio Meteorites: New Insights to Carbonaceous Chondrite (CC) Type Parent Bodies. *Geochimica et Cosmochimica Acta* 251: 217–228.

Horan, M. F., Walker, R. J., Morgan, J. W., Grossman, J. N., and Rubin, A. E. 2003. Highly Siderophile Elements in Chondrites. *Chemical Geology* 196: 5–20.

Hunt, A. C., Ek, M., and Schönbächler, M. 2017. Separation of Platinum from Palladium and Iridium in Iron Meteorites and Accurate High-Precision Determination of Platinum Isotopes by Multi-Collector ICP-MS. *Geostandards and Geoanalytical Research* 41: 633–647.

Jiang, Y., Zhang, X. R., He, W. Z., Liao, S. Y., Herd, C., Peng, J. B., and Hsu, W. B. 2023. Gyarub Zangbo: An Anomalous Carbonaceous Pallasite. 54th Lunar and Planetary Science Conference, abstract #2806.

Kleine, T., Mezger, K., Münker, C., Palme, H., and Bischoff, A. 2004. ^{182}Hf–^{182}W Isotope Systematics of Chondrites, Eucrites, and Martian Meteorites: Chronology of Core Formation and Mantle Differentiation in Vesta and Mars. *Geochimica et Cosmochimica Acta* 68: 2935–46.

Kracher, A., Willis, J., and Wasson, J. T. 1980. Chemical Classification of Iron Meteorites—IX. A New Group (IIF), Revision of IAB and IIICD, and Data on 57 Additional Irons. *Geochimica et Cosmochimica Acta* 44: 773–787.

Kruijer, T. S., Burkhardt, C., Borg, L. E., and Kleine, T. 2022. Tungsten and Molybdenum Isotopic Evidence for an Impact Origin of Pallasites. *Earth and Planetary Science Letters* 584: 117440.

Kruijer, T. S., Burkhardt, C., Budde, G., and Kleine, T. 2017. Age of Jupiter Inferred from the Distinct Genetics and Formation Times of Meteorites. *Proceedings of the National Academy of Sciences of the United States of America* 114: 6712–16.

Kruijer, T. S., Fischer-Godde, M., Kleine, T., Sprung, P., Leya, I., and Wieler, R. 2013. Neutron Capture on Pt Isotopes in Iron Meteorites and the Hf-W Chronology of Core Formation in Planetesimals. *Earth and Planetary Science Letters* 361: 162–172.

Kruijer, T. S., Kleine, T., Fischer-Gödde, M., Burkhardt, C., and Wieler, R. 2014. Nucleosynthetic W Isotope Anomalies and the Hf-W Chronometry of Ca-Al-Rich Inclusions. *Earth and Planetary Science Letters* 403: 317–327.

Lodders, K. 2003. Solar System Abundances and Condensation Temperatures of the Elements. *The Astrophysical Journal* 591: 1220–47.

Lu, Q., and Masuda, A. 1994. The Isotopic Composition and Atomic Weight of Molybdenum. *International Journal of Mass Spectrometry and Ion Processes* 130: 65–72.

McCoy, T. J., Corrigan, C. M., Nagashima, K., Reynolds, V. S., Ash, R. D., McDonough, W. F., Yang, J., Goldstein, J. I., and Hilton, C. D. 2019. The Milton Pallasite and South Byron Trio Irons: Evidence for Oxidation and Core Crystallization. *Geochimica et Cosmochimica Acta* 259: 358–370.

McCoy, T. J., Walker, R. J., Goldstein, J. I., Yang, J., McDonough, W. F., Rumble, D., Chabot, N. L., et al. 2011. Group IVA Irons: New Constraints on the Crystallization and Cooling History of an Asteroidal Core with a Complex History. *Geochimica et Cosmochimica Acta* 75: 6821–43.

Nagai, Y., and Yokoyama, T. 2014. Chemical Separation of Mo and W from Terrestrial and Extraterrestrial Samples Via Anion Exchange Chromatography. *Analytical Chemistry* 86: 4856–63.

Olsen, E. J., Clayton, R. N., Mayeda, T. K., Davis, A. M., Clarke, R. S., and Wasson, J. T. 1996. Mbosi: An Anomalous Iron with Unique Silicate Inclusions. *Meteoritics & Planetary Science* 31: 633–39.

Pernicka, E., and Wasson, J. T. 1987. Ru, Re, Os, Pt and Au in Iron Meteorites. *Geochimica et Cosmochimica Acta* 51: 1717–26.

Regelous, M., Elliot, T., and Coath, C. D. 2008. Nickel Isotope Heterogeneity in the Early Solar System. *Earth and Planetary Science Letters* 272: 330–38.

Rehkämper, M., and Halliday, A. N. 1997. Development and Application of New Ion-Exchange Techniques for the Separation of the Platinum Group and Other Siderophile Elements from Geological Samples. *Talanta* 44: 663–672.

Rusk, B. 2009. Laser Ablation ICP-MS in the Earth Sciences: Current Practices and Outstanding Issues. *Economic Geology* 104: 601–2.

Schaudy, R., and Wasson, J. T. 1972. The Chemical Classification of Iron Meteorites. VI. A Reinvestigation of Irons with Ge Concentrations Lower than 1 ppm. *Icarus* 17: 174–192.

Scott, E. R., Wasson, J. T., and Buchwald, V. F. 1973. The Chemical Classification of Iron Meteorites—VII. A Reinvestigation of Irons with Ge Concentrations between 25 and 80 Ppm. *Geochimica et Cosmochimica Acta* 37: 1957–83.

Scott, E. R. D., and Wasson, J. T. 1976. Chemical Classification of Iron Meteorites-VIII. Groups IC, IIE, IIIF and 97 Other Irons. *Geochimica et Cosmochimica Acta* 40: 103–115.

Spitzer, F., Burkhardt, C., Budde, G., Kruijer, T. S., Morbidelli, A., and Kleine, T. 2020. Isotopic Evolution of the Inner Solar System Inferred from Molybdenum Isotopes in Meteorites. *The Astrophysical Journal* 898: 10.

Tornabene, H. A., Hilton, C. D., Bermingham, K. R., Ash, R. D., and Walker, R. J. 2020. Genetics, Age, and Crystallization History of Group IIC Iron Meteorites. *Geochimica et Cosmochimica Acta* 288: 36–50.

van Nierkirk, D., Greenwoord, R. C., Franchi, I. A., Scott, E. R. D., and Keil, K. 2007. Seymchan: A Main Group Pallasite—Not an Iron Meteorite. *Meteoritics & Planetary Science* 42: 5196.

Vockenhuber, C., Oberli, F., Bichler, M., Ahmad, I., Quittem, G., Meier, M., Halliday, A. N., et al. 2004. New Half-Life Measurement of ^{182}Hf: Improved Chronometer for the Early Solar System. *Physical Review Letters* 93: 172501.

Völkening, J., Köppe, M., and Heumann, K. G. 1991. Tungsten Isotope Ratio Determinations by Negative Thermal Ionization Mass Spectrometry. *International Journal of Mass Spectrometry and Ion Processes* 107: 361–68.

Walker, R. J. 2012. Evidence for Homogenous Distribution of Osmium in the Protosolar Nebula. *Earth and Planetary Science Letters* 351-352: 36–44.

Walker, R. J., McDonough, W. F., Honesto, J., Chabot, N. L., McCoy, T. J., Ash, R. D., and Bellucci, J. J. 2008. Modeling Fractional Crystallization of Group IVB Iron Meteorites. *Geochimica et Cosmochimica Acta* 72: 2198–2216.

Walte, N. P., Solferino, G. D., Golabek, G. J., Silva Souza, D., and Bouvier, A. 2020. Two-Stage Formation of Pallasites and the Evolution of their Parent Bodies Revealed by Deformation Experiments. *Earth and Planetary Science Letters* 546: 116419.

Warren, P. H. 2011. Stable-Isotopic Anomalies and the Accretionary Assemblage of the Earth and Mars: A Subordinate Role for Carbonaceous Chondrites. *Earth and Planetary Science Letters* 311: 93–100.

Wasson, J. T., and Choe, W.-H. 2009. The IIG Iron Meteorites: Probable Formation in the IIAB Core. *Geochimica et Cosmochimica Acta* 73: 4879–90.

Wasson, J. T., and Choi, B.-G. 2003. Main-Group Pallasites: Chemical Composition, Relationship to IIIAB Irons, and Origin. *Geochimica et Cosmochimica Acta* 67: 3079–96.

Wasson, J. T., and Huber, H. 2006. Compositional Trends among IID Irons; their Possible Formation from the P-Rich Lower Magma in a Two-Layer Core. *Geochimica et Cosmochimica Acta* 70: 6153–67.

Wasson, J. T., Huber, H., and Malvin, D. J. 2007. Formation of IIAB Iron Meteorites. *Geochimica et Cosmochimica Acta* 71: 760–781.

Wasson, J. T., and Kallemeyn, G. W. 2002. The IAB Iron Meteorite Complex: A Group, Five Subgroups, Numerous Grouplets, Closely Related, Mainly Formed by Crystal Segregation in Rapidly Cooling Melts. *Geochimica et Cosmochimica Acta* 66: 2445–73.

Wasson, J. T., and Wai, C. M. 1976. Explanation for the Very Low Ga and Ge Concentration in some Iron Meteorite Groups. *Nature* 261: 114–16.

Wittig, N., Humayun, M., Brandon, A. D., Huang, S., and Leya, I. 2013. Coupled W-Os-Pt Isotope Systematics in IVB Iron Meteorites: In Situ Neutron Dosimetry for W Isotope Chronology. *Earth and Planetary Science Letters* 361: 152–161.

Wood, J. A. 1978. Nature and Evolution of the Meteorite Parent Bodies: Evidence from Petrology and Metallurgy. In *NASA, Washington Asteroids (SEE N78–29007 19-91)*, 45–55. Washington, D.C.: NASA.

Worsham, E. A., Burkhardt, C., Budde, G., Fischer-Gödde, M., Kruijer, T. S., and Kleine, T. 2019. Distinct Evolution of the Carbonaceous and Non-Carbonaceous Reservoirs: Insights from Ru. Mo, and W Isotopes. *Earth and Planetary Science Letters* 521: 103–112.

Worsham, E. A., Walker, R. J., and Bermingham, K. R. 2016. High-Precision Molybdenum Isotope Analysis by Negative Thermal Ionization Mass Spectrometry. *International Journal of Mass Spectrometry* 407: 51–61.

Yang, J., Goldstein, J. I., and Scott, E. R. D. 2010. Main-Group Pallasites: Thermal History, Relationship to IIIAB Irons, and Origin. *Geochimica et Cosmochimica Acta* 74: 4471–92.

Zhang, J., Williams, D. B., and Goldstein, J. I. 1993. The Microstructure and Formation of Duplex and Black Plessite in Iron Meteorites. *Geochimica et Cosmochimica Acta* 57: 3725–35.

SUPPORTING INFORMATION

Additional supporting information may be found in the online version of this article.

Data S1.

Table S1. Siderophile element concentrations for individual tracks obtained via LA-ICP-MS.

Table S2. Average siderophile element abundances determined by LA-ICP-MS of IID iron meteorites.

Table S3. Highly siderophile element concentrations of 17 PMG.

Figure S1. CI chondrite normalized HSE abundances of Lieksa compared to the IIC, IID, and IIF magmatic iron meteorite groups, the PES, the ungrouped pallasite Milton, and the PMG.

Figure S2. $^{187}Re/^{188}Os$ versus ΔOs (a) and $^{187}Re/^{188}Os$ versus $^{187}Os/^{188}Os$ (b) for Lieksa, where ΔOs is the parts per 10,000 deviation of Lieksa's $^{187}Os/^{188}Os$ ratio from a 4.56 Ga reference isochron.

Figure S3. Compilation of Ga (ppm) versus Ni (wt%) and Ge (ppm) versus Ni (wt%) for the magmatic iron meteorite groups, ungrouped irons and pallasites, and Lieksa.